Ultra-Small YPO 4 -YAG:Ce Composite Nanophosphors with a Photoluminescence Quantum Yield Exceeding 50%

Yige Yan, Adel Mesbah, Lhoussain Khrouz, Corinne Bouillet, Chantal Lorentz, Nicholas Blanchard, Anne C Berends, Marie Anne van de Haar, Frédéric Lerouge, Michael R Krames, et al.

Spray Coating Experiments: Setups and Methodologies

The latest eBook from Advanced Optical Metrology. Download for free.

Spray Coating Experiments: Setups and Methodologies, is the third in our Thin Films eBook series. This publication provides an introduction to spray coating, three article digests from Wiley Online Library and the latest news about Evident's Image of the Year Award 2022.

Wiley in collaboration with Evident, are committed to bridging the gap between fundamental research and industrial applications in the field of optical metrology. We strive to do this by collecting and organizing existing information, making it more accessible and useful for researchers and practitioners alike.

EVIDENT
OLYMPUS

WILEY

NANO · MICRO small
www.small-journal.com

Ultra-Small YPO_4-YAG:Ce Composite Nanophosphors with a Photoluminescence Quantum Yield Exceeding 50%

Yige Yan, Adel Mesbah, Lhoussain Khrouz, Corinne Bouillet, Chantal Lorentz, Nicholas Blanchard, Anne C. Berends, Marie Anne van de Haar, Frédéric Lerouge, Michael R. Krames, Ovidiu Ersen, Frédéric Chaput,* and Stephane Parola**

Synthesis of high quality colloidal Cerium(III) doped yttrium aluminum garnet ($Y_3Al_5O_{12}:Ce^{3+}$, "YAG:Ce") nanoparticles (NPs) meeting simultaneously both ultra-small size and high photoluminescence (PL) performance is challenging, as generally a particle size/PL trade-off has been observed for this type of nanomaterials. The glycothermal route is capable to yield ultra-fine crystalline colloidal YAG:Ce nanoparticles with a particle size as small as 10 nm but with quantum yield (QY) no more than 20%. In this paper, the first ultra-small YPO_4-YAG:Ce nanocomposite phosphor particles having an exceptional QY-to-size performance with an QY up to 53% while maintaining the particle size ≈10 nm is reported. The NPs are produced via a phosphoric acid- and extra yttrium acetate-assisted glycothermal synthesis route. Localization of phosphate and extra yttrium entities with respect to cerium centers in the YAG host has been determined by fine structural analysis techniques such as X-ray diffration (XRD), solid state nuclear magnetic resonance (NMR), and high resolution scanning transmission electron microscopy (HR-STEM), and shows distinct YPO_4 and YAG phases. Finally, a correlation between the additive-induced physico-chemical environment change around cerium centers and the increasing PL performance has been suggested based on electron paramagnetic resonance (EPR), X-ray photoelectron spectrometry (XPS) data, and crystallographic simulation studies.

1. Introduction

Largely available micron sized crystalline Cerium(III) doped yttrium aluminum garnet ($Y_3Al_5O_{12}:Ce^{3+}$, "YAG:Ce") particles have been successfully used in various light emitting diode (LED)-related applications. The material is perfectly suited for these kind of applications, as it has a strong absorption in the blue spectral region, high quantum yield, and good chemical and physical stability at elevated temperatures.[1,2] However, for the ultra-small colloidal YAG:Ce nanoparticles ("NPs", i.e., with a particle diameter < 50 nm in suspension), meeting the required ultra-small particle size and high photoluminescence (PL) performance (i.e., high photoluminescence quantum yield, "PLQY" or "QY" in short) simultaneously is challenging, as a particle size/crystallinity trade-off has been observed previously.[2–4] In this paper, we refer to particle size as the "hydrodynamic particle size", i.e., the size measured with

Y. Yan, L. Khrouz, F. Lerouge, F. Chaput, S. Parola
Laboratoire de Chimie
ENS Lyon, CNRS, UCBL - UMR 5182
46, allée d'Italie, 69364 Lyon Cedex 07, France
E-mail: yige.yan@ens-lyon.fr; frederic.chaput@ens-lyon.fr; stephane.parola@ens-lyon.fr

A. Mesbah, C. Lorentz
Université de Lyon
Université Claude Bernard Lyon 1
CNRS
IRCELYON—UMR 5256, 2 Avenue Albert Einstein
69626 Villeurbanne Cedex, France

The ORCID identification number(s) for the author(s) of this article can be found under https://doi.org/10.1002/smll.202208055.

DOI: 10.1002/smll.202208055

C. Bouillet, O. Ersen
Institut de Physique et Chimie des Matériaux de Strasbourg
UMR 7504 CNRS-ULP
23 rue du Loess, 67087 Strasbourg, France

N. Blanchard
Université de Lyon
Université Claude Bernard Lyon 1
CNRS
Institut Lumière Matière
69622 Villeurbanne, France

A. C. Berends, M. Anne van de Haar
Seaborough Research BV
Matrix VII Innovation Center
1098XG Amsterdam, The Netherlands

M. R. Krames
Arkesso LLC
Palo Alto, California 94306, United States

DLS that reflects the true size of colloidal particles, including aggregations. Often, high-temperature-annealing yields high crystalline YAG:Ce particles with exceptional high QY,[5] yet in exchange of losing control on the particle size. This drawback hampers the use of this material on emerging techniques like micro-LEDs where YAG:Ce offers superior brightness and color gamut advantages over organic LED (OLED) displays[2,6], or "inter-particle Förster resonance energy transfer"(IFRET)-based technologies that couples sensitizer and emitter ions doped nanocrystals, where lanthanide-based multi-garnet-hosts clearly outperform quantum dots or perovskite emitter materials in terms of temperature robustness of sensitization, emission intensity or peak wavelength.[7] Previous studies[8,9] have tuned the synthesis parameters to reduce the YAG:Ce particle size from 96 nm to as small as 10 nm,[10,11] but unfortunately the QY was also reduced from 50%[12] to less than 20% for these smaller particles.[13] The performance of YAG:Ce NPs fall behind competing ultra-small colloidal luminescent materials like non-oxide chalcogenide quantum dots[14] and perovskites[15] in terms of the QY-to-size performance.

In this paper, we report the first ultra-small YPO_4-YAG:Ce nanocomposite particles having an QY up to 53% while maintaining the particle size ≈10 nm. This is a clear superior QY-to-size performance compared to YAG:Ce-based NPs synthesized by different strategies (**Figure 1** top).[5,8,9,11–13,16–19] Our NPs are produced via a phosphoric acid- and extra yttrium acetate-assisted glycothermal synthesis route (**Scheme 1**). Localization of phosphate and extra yttrium entities with respect to cerium centers in YAG host has been determined by fine structural analysis techniques such as XRD, solid state NMR, and HR-STEM. Finally, a correlation between the additive-induced physico-chemical environment change around cerium centers and the increasing PL performance has been suggested with EPR, XPS data and crystallographic simulation studies.

2. Results and discussion

Sub-10-nanometer colloidal YAG:Ce3% nanocrystals have been obtained by a diethylene glycol (DEG)-assisted glycothermal synthesis in anhydrous condition, as previously reported by our group.[11] The cause of the inhibited particle aggregation formation was attributed to a strong passivation effect of DEG on aluminum isopropoxide, resulting in a more controlled glycolysis-condensation-crystallization process. Even though the particles obtained with this method are ultra-small, the drawback, however, is that the PLQY of those nanoparticles (in dried form) was measured to be only ≈19% (Figure 1 bottom and Figure S1a, Supporting Information). The peak position of the emission spectra excited at 450 nm was located ≈535 nm (**Figure 2**a), which is noticeably blue shifted compared to that of the micron-sized YAG:Ce3% analogue.[20,21] The photoluminescence (PL) decay (Figure 2b) shows a bi-exponential behavior with a fast component of a few nanoseconds, which is also different from micron-sized YAG:Ce3% which has a typical single exponential decay time in the order of a 100 ns. All indications converged to a deteriorated PL performance. A crystallographic analysis of the YAG:Ce3% NPs with ^{27}Al single-pulse excitation (SPE)-MAS solid-state NMR, revealed a ratio of 0.86 when comparing the peak area of tetrahedral Al sites (AlO_4, centered at 50 ppm) to that of octahedral Al sites (AlO_6, centered at 0 ppm, Figure S2, Supporting Information, top). This value is significantly smaller than that of a perfectly crystallized bulk YAG material which has a theoretical ratio of 1.50. This difference indicates a less crystallized YAG host environment compared to micron sized YAG. It could be hypothesized that the lower crystal quality of glycothermally synthesized YAG NPs originates from the lack of a water-participated repair mechanism in the water-deprived reaction medium, resulting in lattice defects.[3] In any case, the lower crystal quality is expected to be the principal reason for the PL performance drawback for YAG nanoparticles synthesized by glycothermal route.[11,18]

In this work, we show that with the addition of an adequate amount of phosphate and an extra yttrium source (i.e, by adding phosphoric acid with a P/Al ratio of 0.054, and yttrium acetate with a Y/Al ratio of 0.8, i.e., 0.2 in excess), the PLQY was significantly increased to near 50% (Figure S1b, Supporting Information) while the particle size was kept around several nanometers. Figure 1 bottom demonstrates the evolution of PLQY and dynamic light scattering (DLS)-measured particle size as a function of P/Al and extra Y/Al ratios in detail. In general, more P added resulted in an increased PLQY and particle size, while an adequate amount of extra Y was needed along with the P addition to keep the particle size small, without significantly impacting the PLQY. The amount of extra Y needs to be higher than is stoichiometrically required to form YPO_4 regarding to the amount of P, but should not be too exaggerated to impact the particle size. An extra Y/P molar ratio equal or smaller than 1.0 resulted in severe particle aggregation, while a too large extra Y/P ratio resulted in decreased PLQY (Table S1, Supporting Information). The most optimal point was found with an extra Y/Al ratio of 0.4 (i.e., a total Y/Al ratio of 1.0) and a P/Al ratio of 0.193, which yielded a PLQY of 53% (Figure S1c, Supporting Information) and a particle size of ≈15 nm. Further addition of P and extra Y in very large excess (i.e., a total Y/Al ratio of 2.0 and a P/Al ratio of 0.4) resulted in a lowered PLQY of 38.9 % and severe particle aggregation (particle size ≈30 nm).

The emission peak center excited at 450 nm for the samples synthesized with an adequate P/Al ratio of 0.054 and 0.193 and Y/Al ratio of 0.8 and 1.0 appeared at ≈553 nm, meaning a 15 nm shift toward longer wavelengths (Figure 2a) compared to that of the additive-free bare YAG:Ce3% NPs (labeled as "bare YAG:Ce3%"), and was close to that of the micron-sized material (≈555 nm, an example of a such material is shown in Figure S3, Supporting Information). Also, the PL decay showed an almost mono-exponential decay with suppression of the shortest component (Figure 2b). All above indicators suggested a physico-chemical environment variation has been induced around the Ce^{3+} optical active centers in the host structure,[22] which will be discussed in detail later.

The Ce/Al ratio (0.018±0.002 for bare YAG:Ce) were not significantly influenced by the addition of extra Y and P addition, and the values was close to the targeted 3%Ce compared to the Y (excluding extra added Y, Ce/Al = 0.017±0.002 for the nanocomposite with a total Y/Al ratio of 0.8 and a P/Al ratio of 0.054) (Table S2, Supporting Information). The presence of the P in NPs was clearly evidenced in the fourier transform infrared (FTIR) pattern (**Figure 3**a) by the group of peaks

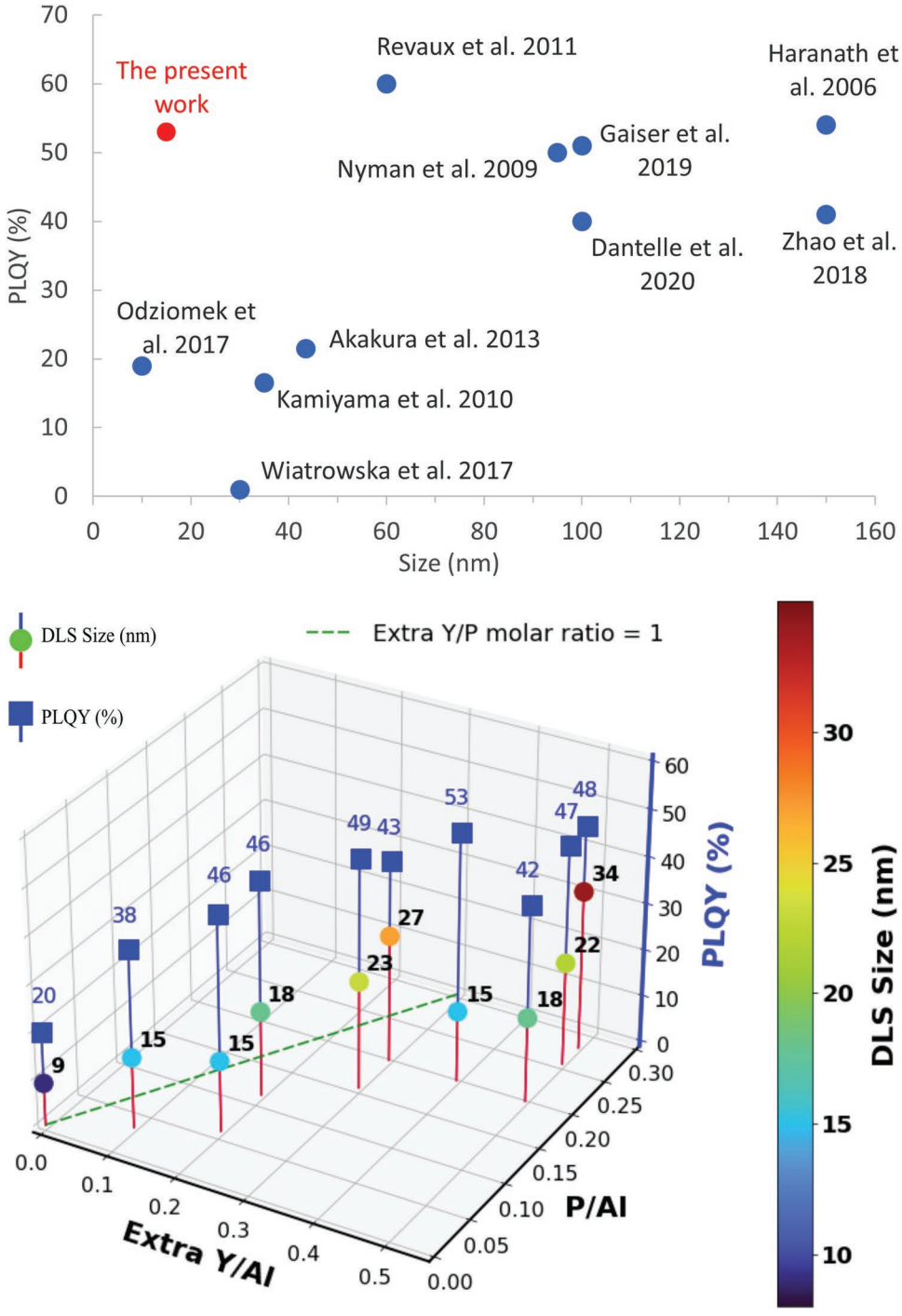

Figure 1. (Top) State of art comparison of YAG:Ce-based nanophosphors synthesized with different strategies[5,8,9,11–13,16–19] in terms of the PL performance versus particle size. (Bottom) PLQY (%) and particle size measured by DLS of YAG:Ce3% NPs synthesized with different P/Al and Extra Y/Al molar ratios. The Extra Y refers to the excess Y entities besides of those designated to form stoichiometrically YAG with Al entities.

between 1012 and 1120 cm^{-1}, which can be attributed to the P—O bond which is typically in the energy range of different orthophosphate (PO_4) forms,[23] which is even witnessed in case of small extra Y and P addition (i.e., a total Y/Al ratio of 0.8 and a P/Al ratio of 0.054). The broad P-O bands observed in the FTIR patterns, indicate the presence of different P—O chemical environments, usually found in a poorly crystallized state, sometimes referred to as mobile phosphates.[24] The presence of P-related entities can be further supported by the confirmed P signal by energy dispersive X-ray (EDX) measurements (Table S2 and Figure S4, Supporting Information), although hardly observable in XRD pattern (Figure 3b) and HRTEM images (**Figure 4**a,b) which might be due to its small quantity or amorphous nature of the material. Same as

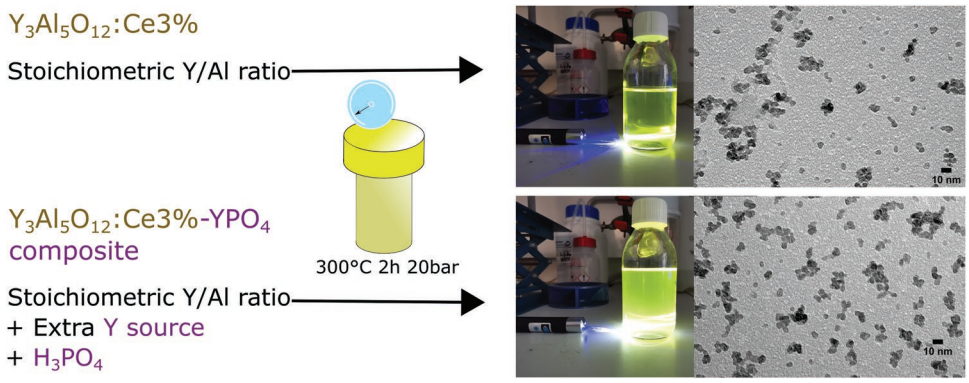

Scheme 1. Comparison of photoluminescence and morphology of the glycothermally prepared bare YAG:Ce3% colloidal suspension by (upper route) adding stoichiometric Y/Al ratio, and that by (lower route) additionally adding moderate amount of extra Y and PO_4^{3-} sources. The conventional glycothermal synthesis of YAG:Ce3% NPs consists of heating a stoichiometric mixture of Aluminum isopropoxide ($Al(^iPrO)_3$), Yttrium acetate ($Y(OAc)_3$) and Cerium acetate ($Ce(OAc)_3$) in a solvent mixture of 85%v 1,4-Butanediol and 15%v Diethylene glycol (DEG), for 2 h at 300 °C in an autoclave.

the confirmed P presence, the EDX measurements confirmed the presence of Y in an excess quantity as expected. Larger amount of extra Y and P addition (i.e., a total Y/Al ratio of 1.0 and a P/Al ratio of 0.193) induced further structural changes as is clear from the peaks related to PO_4 in the FTIR spectra that evolved into a more single-component peak at 1012 cm^{-1} (Figure 3a), indicating a more crystallized PO_4-based environment. The nature of this crystalline phase was revealed by the appearance of two peaks situated ≈25.8 and 51.7° 2-theta (XRD, Figure 3b), identified as Yttrium (III) phosphate (monazite type tetragonal YPO_4, JCPDS 00-011-0254) phase according to the JCPDS database. HRTEM images confirmed

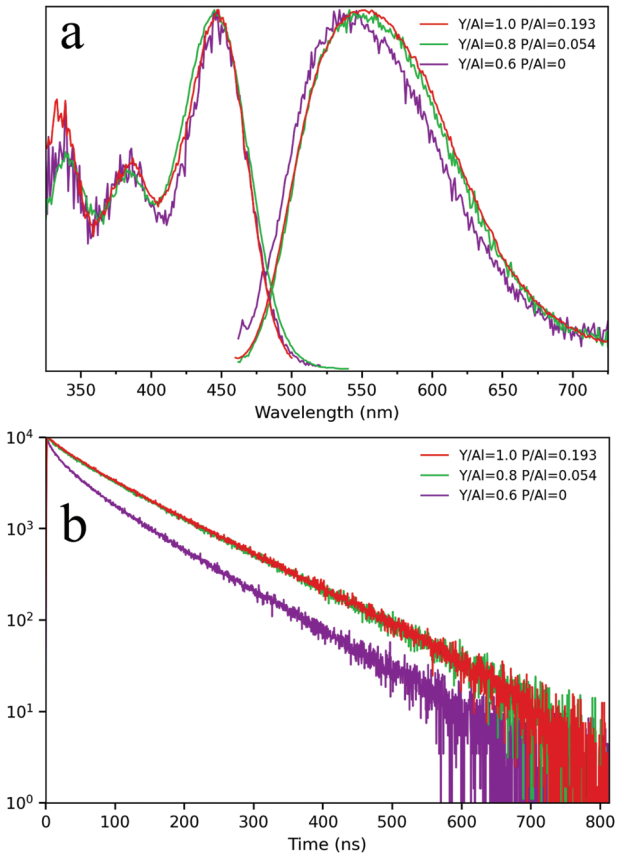

Figure 2. a) Normalized photoluminescence emission spectra excited at a wavelength of 450 nm and b) photoluminescence decay excited at a wavelength of 440 nm of the YAG:Ce3% NPs synthesized with different Y/Al molar ratios (0.6, 0.8, and 1.0) and different P/Al molar ratio (0, 0.054, and 0.193).

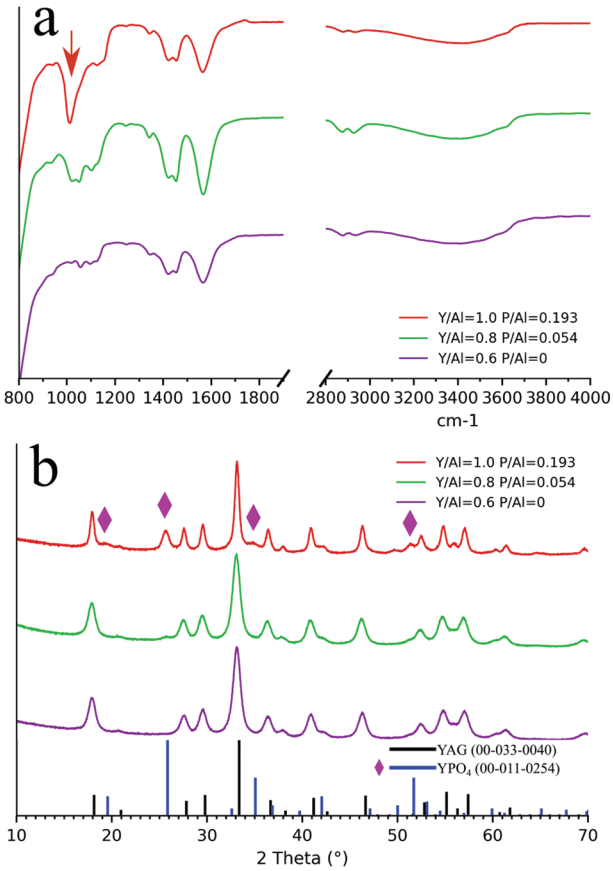

Figure 3. a) XRD patterns (purple diamonds marks are assigned to the YPO_4 phase), b) FTIR analysis (the red downward arrow indicates the P—O bond) of the YAG:Ce3% NPs synthesized with different Y/Al molar ratios (0.6, 0.8, and 1.0) and different P/Al molar ratio (0, 0.054, and 0.193).

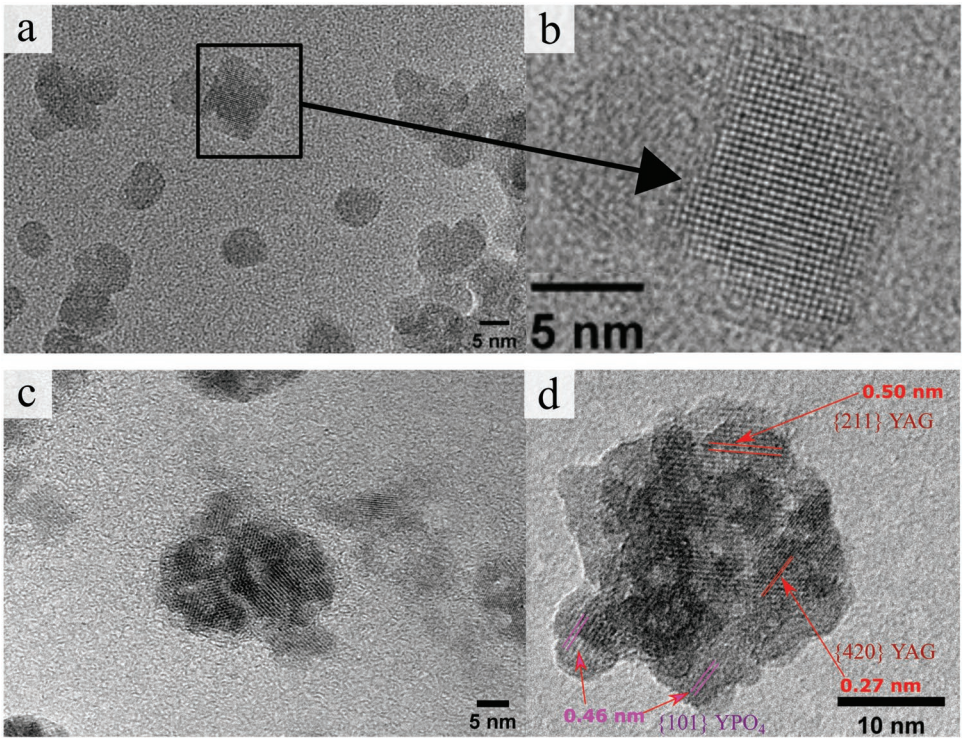

Figure 4. a,b) Typical TEM and HRTEM image of the YAG:Ce3% NPs synthesized with a Y/Al molar ratio of 0.8 and P/Al molar ratio of 0.054. c,d) Typical TEM and HRTEM images of YAG:Ce3% NPs synthesized with a Y/Al molar ratio of 1.0 and a P/Al molar ratio of 0.193, showing the presence of YPO_4 (lattice spacing d = 0.46 nm) and YAG phase (d = 0.50 and 0.27 nm).

the simultaneous presence of lattice planes for YPO_4 and YAG phase intimately associated at nanoscale (Figure 4c,d), forming a composite structure. Large amount of extra Y and P addition resulted in a slight increase to the primary YAG crystallite size, as well as an increase in actual particle size (Table S2, Supporting Information). The former is possibly a result of an accelerated nucleation-crystallization process of YAG with the presence of an acid (H_3PO_4). The latter is probably due to aggregations favored by the chelating effect of surface PO_4. Nevertheless, it seems that only a small amount of extra Y and P addition was able to significantly improve the PLQY. Further addition of additives did not alter PLQY in a great manner, despite resulting in different NPs morphologies and state of YPO_4.

The location of the added P and extra Y with respect to the YAG:Ce3% NPs as well as the mechanism of YPO_4 formation was revealed by kinetically following the crystallinity of YPO_4 species with increasing synthesis length. With a small addition of P and extra Y (i.e., a P/Al molar ratio of 0.054 and a Y/Al molar ratio of 0.8), the XRD peak intensity of the tetragonal YPO_4 phase increased with the reaction length from 2 to 8 h respectively (Figure S5a, Supporting Information), while the peaks corresponding to YAG phase did not change significantly. This suggests that the crystallization process of the YAG phase is effectively finished at 2 h, possibly after reaching a crystallization-redissolution equilibrium, while the crystallization of YPO_4 phase starts at a significantly later stage. In agreement with this hypothesis, the FTIR kinetic study showed that the intensity of the peak located at 1012 cm^{-1} for crystalline PO_4 species was increased from 2 to 8 h, dependent on the reaction time (Figure S5b, Supporting Information). The elemental analysis by EDX spectroscopy in SEM (Table S3, Supporting Information) showed that both the rare earth elements to Al and P/Al ratios did not change significantly with reaction length. It further supports that the totality of those additional Y and P entities were already present on/in crystallized YAG:Ce3% NPs at the early stage of the reaction. Then, for longer reaction times, these additional species crystallize into YPO_4. ^{27}Al single pulse excitation (SPE)-magic angle spinning (MAS) NMR (**Figure 5**a) show similar spectra regardless of the reaction length, suggesting similar overall YAG crystallinity (the AlO_4/AlO_6 ratio was 1.19 after 2 h (Figure S2, Supporting Information) and 1.13 after 8 h reaction). But the cross-polarization (CP)-MAS ^{27}Al NMR spectra (Figure 5a), which provide information about the chemical environment around Al located on the surface of the sample (i.e., Al atoms at fixed distance with Hydrogens atoms which can be found only in surface ligands, expected to be in AlO_6 form), showed a clearer shift of peak position toward lower ppm value with the increasing reaction length. Our hypothesis is that the longer reaction time could finalize the crystallization process of the YAG phase, though marginally. This is correlated with a diminishing ^{27}Al NMR peak located between 5 and 6 ppm, corresponding to Al in a reportedly glycol derivative of boehmite phase, which is often considered as a non-finished by-product in glycothermal synthesis of YAG.[11,25] ^{31}P SPE- and CP-MAS NMR spectra (Figure 5b) showed similar broad shapes at 2 h reaction time, suggesting that the majority of PO_4 species is in

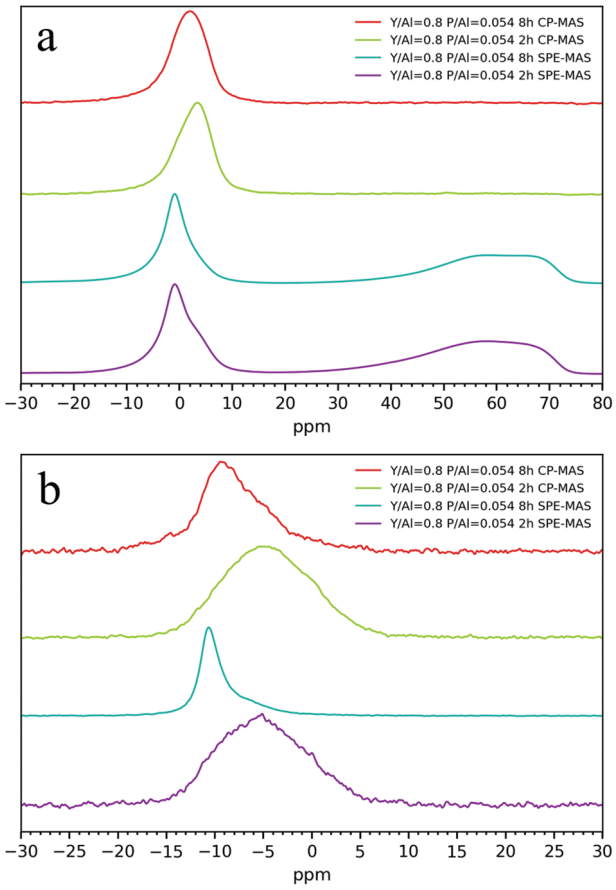

Figure 5. a) Comparison of ^{27}Al SPE-MAS and CP-MAS solid state NMR spectra and b) ^{31}P SPE-MAS and CP-MAS solid state NMR spectra of the YAG:Ce3% NPs synthesized with different reaction times (2 h, 8 h), the Y/Al molar ratio was 0.8 and the P/Al molar ratio was 0.054.

non-crystalline form. However, increasing the reaction time to 8 h drastically sharpened the peak shape for both ^{31}P SPE- and CP-MAS NMR spectra, and the peak center has moved toward −11.4 ppm which is the resonance of ^{31}P in crystalline tetragonal YPO_4 phase.[26] All indicates that the extra Y and P species have been partially crystallizing into YPO4 slowly throughout the 2-8 h window, with a small portion of Y-PO_4-species stayed at a mobile state, dispersed inside of the YAG host. Just to mention, large amounts of extra Y and P addition (e.g., Y/Al = 1.0 and P/Al = 0.193) have resulted in similar increased crystallinity for both YAG and YPO_4 domains, while requiring a shorter reaction time (Figure S2, Supporting Information bottom). Although the crystallinity of YPO_4 was improved with higher amount of additive addition, mobile YPO_4 species always existed. YPO_4 species near Ce centers are expected to affect the PL properties of the nanocomposite. But the PL property can be affected as well in other situations, they are discussed first in below: Supposing that a significant amount of Ce^{3+} is found in crystalline YPO_4 phase could result in a dilution of the effective amount of Ce in the YAG host, thus leading to an increase of the PLQY. However, this scenario is excluded. The characteristic emission of Ce^{3+} in YPO_4 host excited by UV[27] was detectable only when the added amount of extra Y and P was large enough to form crystalline YPO_4 (Figure S6, Supporting Information, top). Small amount of extra Y and P addition resulted in a negligible amount of crystalline YPO_4 environment, thus no detectable Ce^{3+} emission in YPO_4, yet already yielded a high PLQY of 46%. In addition, the intensity of the emission (exited at 450 nm) of a 1%w aqueous suspension of YAG:Ce-PO_4 nanocomposite with small amount of extra Y and P addition is nearly twice as high as that of the 1%w additive-free YAG:Ce suspension (Figure S6, Supporting Information, bottom). In another scenario, Ce ions associated with PO_4^{3-} are expected to be restrained at an oxidation state of (III) instead of (IV).[28] This could be thought as another cause to the increased PLQY as if the presence of P limits the formation of Ce(IV) which is a PL quencher. However, this scenario is also excluded because Ce_{3d} XPS spectra of the NPs (**Figure 6**a) showed predominate Ce(III) signals regardless of the addition of extra Y/P or not (the signal for Ce(IV) at 917 keV is absent). This finding is in contrast to many observations, as traces of Ce(IV) have been found numerously for YAG:Ce-based material prepared by wet-chemical routes. But our material was synthesized under reducing environment, and it is known that glycothermal route yields predominantly Ce(III) for YAG:Ce.[19,29] Furthermore, the product was only very shortly exposed to air, only during the solid recovery and washing, after which the samples were stored in an Argon atmosphere without annealing. Thus, oxidation should have largely been prevented.

With above possible PL-alteration scenarios have been eliminated, an EPR study at liquid He temperature has been performed to investigate a possible change of the physico-chemical environment around Ce centers by the presence of additives. Figure 6b shows the EPR spectra in perpendicular mode of YAG:Ce3% NP powder synthesized with different amounts of extra Y and P. Three main resonance signals are detected at this temperature. The absence of these signals at room temperature allows us to exclude the possibility that they originate from the oxygen defects. Thus, we believe that the EPR results are representative of the physico-chemical environment around Ce(III). The species Ce1 in the bare YAG:Ce3% sample was found with a g_{av} = 2.1 ($g_{//}$ = 2.7, $g_{\perp}$ = 1.8). This specie disappeared gradually with increasing P and extra Y addition to near total disappearance. Meanwhile, the second specie Ce2 with a g_{av} = 3.1 (g_1 = 3.9, g_2 = 3.1, g_3 = 2.4) emerged strongly with increasing P and extra Y addition in both samples. On the other hand, the broad peak at g_{av}≈1.3 could be explained by existence of a dipolar interaction of a new Ce3 species. The parallel mode of EPR signals approving this assumption is shown in Figure S7 (Supporting Information). Nevertheless, the attribution of this peak is uncertain due to the lack of literature reference, and therefore is not subject to discussion in this paper. From this data we conclude that the addition of extra Y and P has at least converted the environment of Ce from Ce1-type to Ce2-type, suggesting a transition in chemical coordination numbers[30] or physical distortion environments.[31] The former could be a result of an intimate contact between Ce and PO_4 species, since the coordination number of the Ce in a monazite structure is 9 instead of 8 if Y is partly substituted by Ce.[32,33] The latter distortion could be a result of an internal dispersion of PO_4 inside of YAG host. In order to confirm the inclusion of Ce and PO_4 and also the role of excess Y in the YAG lattice, long-scanned PXRD data were collected on Ce-free YAG and YAG:Ce3% NPs

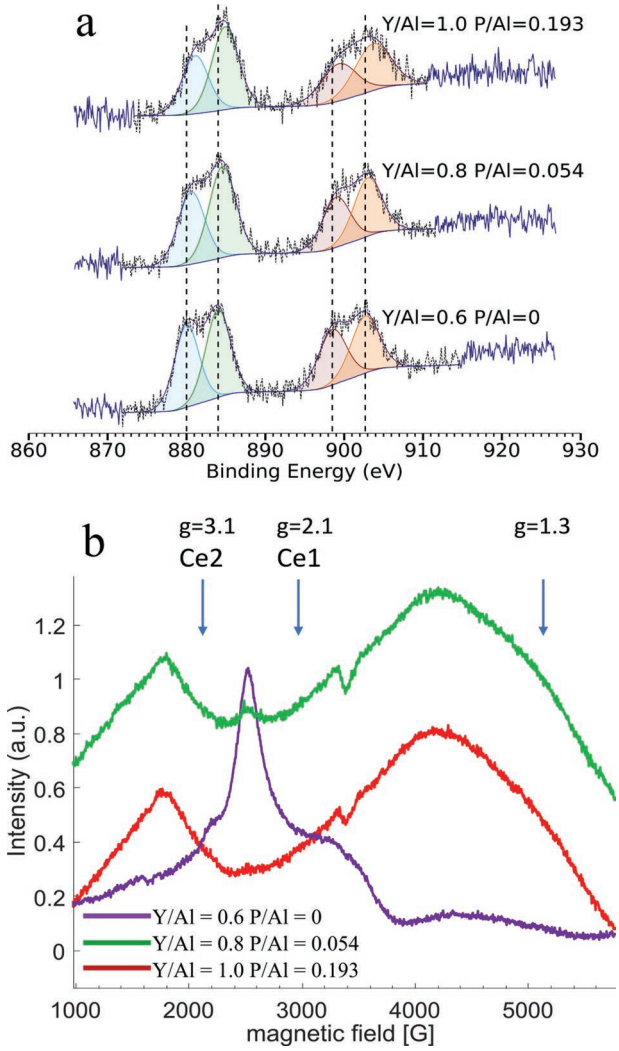

Figure 6. a) XPS Ce_{3d} spectra and b) EPR spectra in perpendicular mode of the YAG:Ce3% NPs synthesized with different Y/Al molar ratios (0.6, 0.8, and 1.0) and different P/Al molar ratios (0, 0.054, and 0.193). The EPR results showed the evolution of different populations of Ce centers.

synthesized with different P/Al and Y/Al atomic ratios. The refined unit cell parameters are reported in **Table 1**.

From the obtained results, Ce-free bare YAG shows a larger unit cell volume than those reported in the literature of ≈10 Å^3 with V = 1744.55(6) Å^3 instead of 1730.7(2) Å^3,[34] such behavior can be explained by the incorporation of small molecular entities within the structure or on the surface leading to a strain effect responsible of a larger volume. The inclusion of organic solvent molecules inside of the glycothermally synthesized gallium garnet particles has been reported before.[35] The calcination at 1000 °C allows the elimination of such impurities and defects, leading to a volume of 1732.22(1) Å^3, close to those reported in the literature for micron sized YAG.[35] The YAG NPs synthesis in the presence of P and extra amount of Y further led to a change of the unit cell parameters, which could be explained by three different mechanisms (**Figure 7**) detailed as follows:

1) The incorporation of cerium ions increases the unit cell volume, they are incorporated in the YO_8 with a larger ionic radius (Ce^{3+} = 1.143 Å , Y^{3+} = 1.019 Å , see Shannon tables[36]).

2) The use of an excess amount of Y during the synthesis increases the unit cell volume, this is explained by the partial substitution of aluminum octahedral site AlO_6 (−3. Symmetry site) and in agreement with their respective ionic radius (rAl^{3+} = 0.535 Å, rY^{3+} = 0.9 Å).

3) The use of phosphates seems to lower the unit cell volume. This is assumed to be a consequence of partial substitution of the aluminum atoms (rAl^{3+} = 0.3 Å) in the tetrahedral site (−4. symmetry site) by phosphorus atoms (rP^{5+} = 0.17 Å). Moreover, in order to ensure the charge balance, we suggest that five aluminum atoms are replaced by three phosphorus atoms and 2 vacancies (□) as follows: $5Al^{3+} \leftrightarrow 2P^{5+}$ + 2 □. It is worth noting that there is a limit of substitution of phosphates close to 10%.wt based on the estimated number of substitutable AlO_4 site per cell unit, above this value the excess of phosphates forms the xenotime structure YPO_4 (tetragonal, $I4_1/amd$). Similar phenomenon has been reported elsewhere.[37]

In addition of the refined unit cell parameters values, the Rietveld refinement by Fullprof_Suite allowed the extraction of the crystallite size and micro-strain effect of YAG:Ce samples (Figure S8, Supporting Information). The incorporation of

Table 1. Cell parameter and cell volume calculated by crystallographic simulation of the Ce-free YAG and YAG:Ce3% NPs synthesized with different P/Al and Y/Al atomic ratios.

Sample	P/Al atomic ratio	Y/Al atomic ratio	Cell parameter [Å]	Cell volume [Å^3]
Ce-free YAG	0	0.6	12.0382(2)	1744.55(6)
Ce-free YAG 1000 °C	0	0.6	12.0098(2)	1732.22(1)
YAG:Ce3% 2h	0	0.6	12.0560(1)	1754.01(4)
YAG:Ce3% 2 h 1000 °C	0	0.6	12.0152(1)	1734.58(1)
YAG:Ce3% Y0.6P0.054 2h	0.054	0.6	12.0328(1)	1742.19(3)
YAG:Ce3% Y0.8P0.054 2h	0.054	0.8	12.0822(1)	1763.76(4)
YAG:Ce3% Y0.8P0.108 2h	0.108	0.8	12.0610(1)	1755.78
YAG:Ce3% Y0.8P0.054 2 h 1000 °C	0.054	0.8	12.0429(1)	1746.60(2)

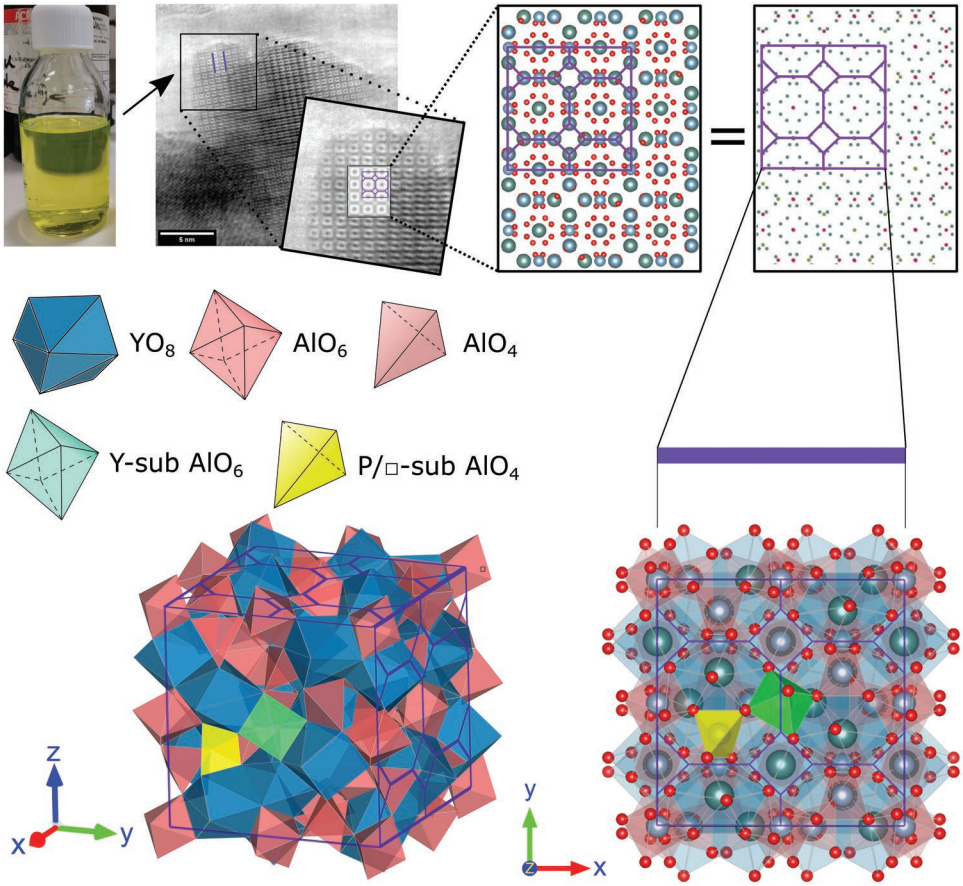

Figure 7. Crystallographic simulation of YAG:Ce3% NPs synthesized with large extra Y and P addition (Y/Al=1.0, P/Al=0.193) based on HRTEM and PXRD data. (Top left) NP suspension in reaction medium after synthesis. (Top middle) HRTEM projection of a particle in the [001] zone axis. (Top right) a multislice simulation done with the JEMS software for a ≈2 nm thick particle. (Bottom right) the computational generated crystal structure in the [001] zone axis and in 3D view (Bottom left) showing the possible substitution modes of Y by Ce and Al by P or vacancies in a unit cell based on PXRD analysis. The unit cell frame was drawn based on the PXRD data and was highlighted in the top right pictures.

phosphates and the increase of the Y/Al ratio seems to favor the increase of the crystallite size of the YAG host while reducing defects. This slight increase of crystallinity for the YAG host is in accordance with the earlier suggested faster nucleation rate of YAG:Ce3% NPs in presence of extra Y and P addition. But the increased host crystallinity is thought to be not the main contributing factor to the increased PL performance. Indeed, the PXRD refinement as well as the EPR reveal that the dispersion of P and extra Y as foreign atoms has induced a structure distortion on the YAG host. According to the conclusion drawn by Ueda et al. and others,[38,1] we believe that the change of the local Ce^{3+} environment was caused by a change of electronic structure around Ce centers via the distortion of the host by the addition of a small amount of P and extra Y, which is responsible for the altered the PL properties. This electronic structure change can be evidenced by the increasing shift of Ce_{3d} peaks toward the higher binding energy, which begins with a small quantity of extra Y and P addition in the XPS spectra (Figure 6a), possibly caused by a change of electronegativity of nearby atoms of Ce when a substitution of atoms occurs.[39] The fact that only a small amount of additional Y and P is sufficient to obtain a high PLQY suggests that the dispersed Y-PO_4-species near Ce are the main factor influencing the PL, rather than the crystalline YPO_4 phase.

A direct observation of the localization of P-related entities regarding to the NPs is difficult. Although by correlating the EPR spectra and PXRD analyses, we believe that the extra Y and additional P exist in two different forms in the YAG-YPO_4 nanocomposites depending on their quantity. A low concentration of additives yields dispersed Y-PO_4-species with close contact/interaction with Ce centers; while for a high concentration, besides dispersed Y-PO_4, part of Y-PO_4-species form monazite-type crystalline structure preferentially on the surface of YAG:Ce NPs and merged into a larger network. The presence of the latter relies on the analysis of the HRTEM images and EDX elemental maps (**Figure 8**) for heavily P- and extra Y-added sample; indeed, it seems that the sub-10 nm YAG-rich region dots are incorporated inside a continues network constructed by Y- and P-rich crystalline YPO_4 regions. We think that the distortion applied to YAG host is mainly resulting from the dispersed YPO_4 species, not from the crystalline YPO_4, since monazite and YAG crystalline phase are reported epitaxial compatible,[40] and therefore the strain in the crystal boundaries is expected to be limited. It is worth mentioning that all the afore-synthesized

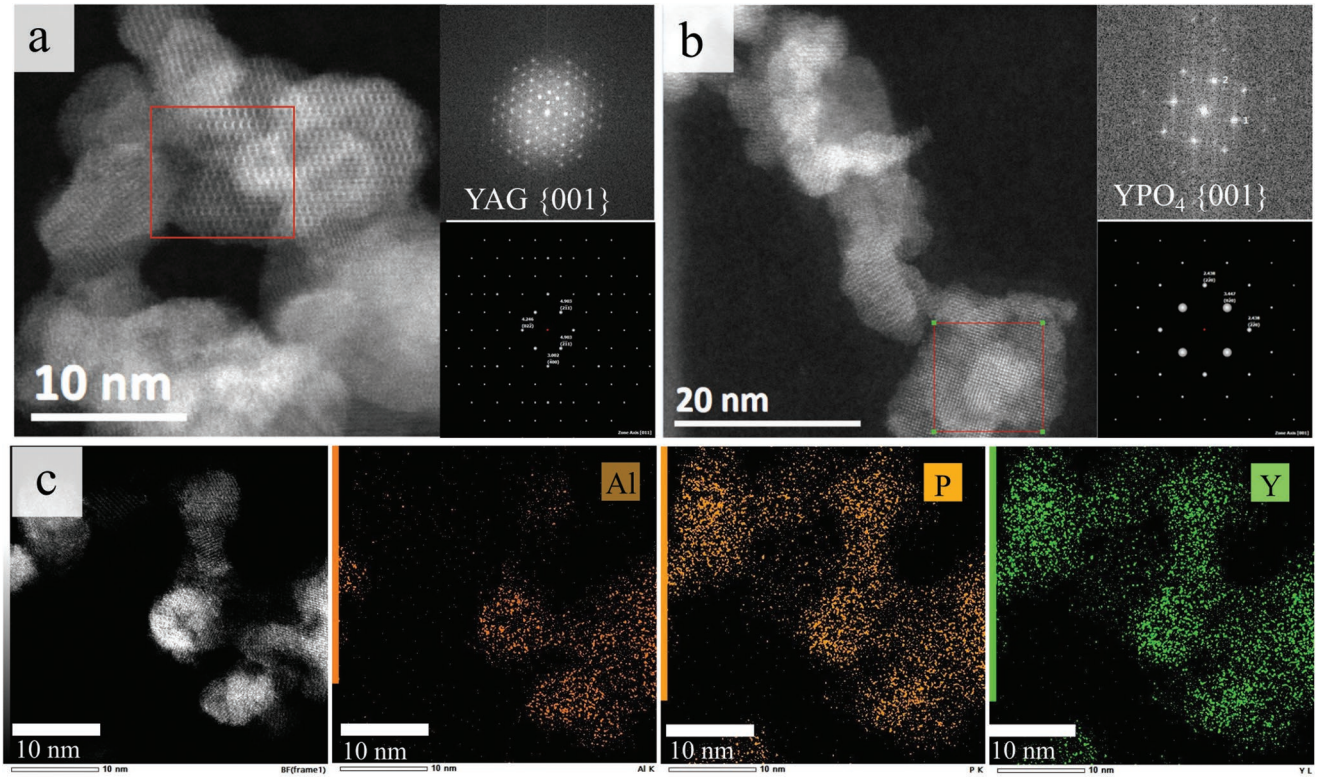

Figure 8. a) High-angular annular dark field (HAADF) STEM image of YAG:Ce3% NPs synthesized with a Y/Al molar ratio of 1.0 and a P/Al molar ratio of 0.193. The FFT pattern of the selected region, which is in good agreement with the structural characteristics of the YAG phase, is shown on the right. b) HAADF STEM image of YAG:Ce3% NPs synthesized with a Y/Al molar ratio of 1.0 and a P/Al molar ratio of 0.193. The insert is the FFT pattern of the selected region, in agreement with the presence of YPO_4 phase. c) STEM-EDX elemental mapping for Al, Y, and P of YAG:Ce3% NPs synthesized with a Y/Al molar ratio of 1.0 and a P/Al molar ratio of 0.193.

NPs slowly lose their PL intensity over time in aqueous suspension or when exposed to air without receiving any irradiation. But with a heavy addition of extra Y and P, this diminishing PL was partially inhibited. We suspected that the crystalline YPO_4 network played a protection role for the nanocomposite NPs. Nevertheless, the exact mechanism behind this quenching behavior and the protective effect of YPO_4 will be detailed in a dedicated paper.

3. Conclusion

In this study, we have overcome the PLQY-to-size performance challenge regarding to the YAG:Ce material by having developed for the first time a colloidal YPO_4-YAG:Ce3% composite nanophosphor material that exhibits simultaneously a high PLQY, of over 50%, and a small (<20 nm) particle size. With adequate quantities of P and extra Y addition, the novel composite showed excellent dispersity with bright yellow Ce^{3+} emission upon blue light excitation. Along with the improved internal YAG host crystallinity by P and extra Y addition, the additive-resulted change of physico-chemical environment around Ce centers is thought to be the main beneficial factor. This discovery of great importance regarding to the synthesis of garnet-type nanophosphors with both ultra-fine particle size and excellent PL performance provides solid assets for realizing highly efficient IFRET technique. We also hope that this work can revamp interests for this kind of material by offering competitive solutions facing quantum dots and perovskites in competing lighting or display applications.

4. Experimental Section

Sample Preparation: The synthesis of YAG:Ce^{3+}-YPO_4 ultra-fine nanophosphors was carried out by a H_3PO_4-assisted glycothermal route with varying Al/Y/P ratios. Pure YAG:Ce^{3+} was synthesized as reference following a typical protocol presented by Odziomek et al.:[11] 20 mmol of distilled aluminum isopropoxide (98%, Sigma Aldrich) was stoichiometrically mixed with 11.6 mmol of dried yttrium acetate (99.9%, Sigma Aldrich) and 0.36 mmol of cerium acetate corresponding to 3% doping (99.9%, Sigma Aldrich) in 200 mL of glycol solvent composed of 15% v/v diethylene glycol (DEG, 99.9%, Sigma Aldrich) and 85% v/v 1,4-butanediol (1,4-BD, 99.9%, Sigma Aldrich). Homogenization of the solution was facilitated using an Ultra-Turrax homogenizing probe. The beaker with the reaction mixture was transferred into a 700 mL autoclave with an additional 60 mL of 1,4-butanediol in the gap between the autoclave and the beaker. The autoclave was purged with N_2 and heated up to 300 °C (3 °C min^{-1}) under constant mechanical stirring (set to 100 rpm – round per minute) and kept at this temperature for 2 h. The autoclave was cooled down to room temperature overnight and opened the next day. The obtained colloidal solution was extremely stable. To promote precipitation, anti-solvents such as a mixture of acetone and diethyl ether were added before centrifugation (19 000 rcf – relative centrifugal force). The whole washing procedure was repeated 2 times

Table 2. Sample table.

Label	Duration (h)	P/Al Atomic ratio	Y/Al Atomic ratio
YAG:Ce3% 2h	2	0	0.6
YAG:Ce3% Y0.8P0.054 2h	2	0.054	0.8
YAG:Ce3% Y0.8P0.054 4h	4	0.054	0.8
YAG:Ce3% Y0.8P0.054 6h	6	0.054	0.8
YAG:Ce3% Y0.8P0.054 8h	8	0.054	0.8
YAG:Ce3% Y1.0P0.193 2h	2	0.193	1.0

before the YAG nanoparticles were re-dispersed in distilled water. A part of the colloidal solution was dried at room temperature for 1 h for further analyses. The YAG nanoparticles sample obtained following this protocol, served as reference sample and was labeled "YAG:Ce3% 2h". The influence of the addition of H_3PO_4 (pure, Sigma Aldrich) at different P/Al atomic ratio, the Y/Al precursor molar ratio as well as reaction length were parameters to be investigated. The mass of the H_3PO_4 and extra Yttrium acetate added in the reaction were adjusted depending on the targeted P/Al and Y/Al ratios. The resulted P-free and P-assisted sample labels and their respective targeted atomic ratios were shown in **Table 2**.

Characterization—XRD: Phase analysis of dried powders was conducted with an Empyrean X-ray diffractometer (Malvern Panalytical) using CuK$\alpha_{1,2}$ radiation in the Bragg-Brentano. Data were collected between 5 and 120 ° in 2θ with a total counting time ≈3 h. The crystal structure of each compound was refined using the Rietveld method over the use of the Fullprof_Suite package.[41] Pure silicon was also collected to extract the instrumental function. During the refinement different profile and structure parameters were allowed to vary such as the zero shift, unit cell parameters, and atomic thermal displacement parameters. The broadening of the diffraction peaks caused by the microstructural effect was refined by the use of both anisotropic size and strain model. The plot corresponding the refinement of the YAG:Ce3% Y0.8P0.054 2 h sample showing the observed, calculated, and the difference patterns was shown in Figure S9 (Supporting Information).

Characterization—DLS: Dynamic light scattering (DLS) was performed to measure the hydrodynamic size of NPs by a Malvern Zetasizer nano series device. In a disposable cuvette, dried NPs were suspended in distilled water with a concentration ≈0.1%w. The hydrodynamic size in number was recorded as an average of three measurements.

Characterization—Electron Microscopy: The morphology and microstructure were studied using a Tecnai Osiris transmission electron microscope (TEM). The elemental analyses of powder samples were studied using a Zeiss Supra 55VP SEM coupled with EDX detector. *Scanning transmission electron microscopy (STEM) imaging and energy dispersive X-ray spectroscopy (EDX)*. Experiments were performed using a JEOL 2100 FEG S/TEM microscope operated at 200 kV equipped with a probe spherical aberration corrector. The samples were deposited on a holey carbon coated TEM grid. For the acquisition of high-angular annular dark field (HAADF) images, a spot size of 0.13 nm, a current density of 140 pA, a camera focal length of 8 cm which corresponds to inner and outer diameters of the annular detector of 73 and 194 mrad, have been used. Elemental maps were obtained in the STEM mode by energy dispersive X-ray spectroscopy (EDX) using a silicon drift detector (SDD) with a sensor size of 60 mm^2.

Characterization—FTIR: Fourier transform infrared spectroscopy (FTIR) of the powders was performed using an attenuated total reflectance (ATR) technique within the 600–4000 cm^{-1} range using an IR spectrometer Spectrum 65 made by Perkin Elmer.

Characterization—Optical Characterization: The photoluminescence spectra were recorded with a Horiba Jobin Yvon Fluorolog-3s spectrofluorometer equipped with a three-slit double-grating excitation and emission monochromator. Emission spectra were recorded with excitation at a wavelength of 450 nm; excitation spectra were recorded by fixing the emission at a wavelength of 550 nm, both on a dried powder filled in a capillary with a 1 nm slit size. The quantum yield (PLQY) of the solid samples had been measured by an absolute method using an integration sphere (GMP® G8 Quantum Integration Sphere). Briefly, an adequate amount of power was sealed in a quartz tube in Ar atmosphere, and it was placed into the integration sphere with minimum diaphragm opening. The tip position of the sample tube was optimized to align with the incident laser and the amount of powder was adjusted to cover the entire illumination region. 4 measurements were conducted to record the absorption and emission spectra with and without the sample tube, and the PLQY was calculated via the formula (1). The lamp aging factor was also taken account, though it was negligible for the duration of these experiments.

Formula (1):

$$\mathrm{PLQY}(\%) = \frac{Ec - Ea}{(La - Lc)/a} \quad (1)$$

Where:

Ec is the intensity integration of the emission spectrum with the presence of sample

Ea is the intensity integration of the emission spectrum without the presence of sample

La is the intensity integration of the absorption spectrum without the presence of sample

Lc is the intensity integration of the absorption spectrum with the presence of sample

a is the transmission percentage of the filter used

Characterization—EPR: Electron paramagnetic resonance spectroscopy (EPR) assays were all carried out at Helium temperature (T = 21 K) using a Bruker EMX spectrometer operating at X-band with standard cavity. The instrument settings were as follows: 100 kHz modulation frequency, 6.5-22 mW microwave power, 5 G modulation amplitude, 20.48 ms time constant.

Characterization—XPS: X-ray photoelectron spectrometry (XPS) analysis was conducted using a Kratos Axis Ultra DLD with monochromatic Al (1486.6 eV) X-Ray source operated at 12 kV x 15 mA = 180 Watts. The survey spectra were recorded in the range from 1200 to 0 eV, with a Pass Energy of 160 eV. High-resolution spectra were recorded for $Ce_{3d5/2\text{-}3/2}$, $Y_{3d5/2\text{-}3/2}$, and other photoemission peaks with a Pass Energy of 40 eV. The charge neutralization was done with a low energy electron beam. The spectra were calibrated using the C_{1s} (C—C, C—H) photoemission peak at 284.8 eV in binding energy.

Supporting Information

Supporting Information is available from the Wiley Online Library or from the author.

Acknowledgements

Y.Y. conceptualized, synthesized, and characterized the nanoparticles, participated to the manuscript writing, A.M. resolved the crystallographic structure, L.K. did the EPR, C.B., N.B., O.E. contributed on the electron microscopy experiments, C.L. the solid-state NMR, A.C.B, M.A.H., M.R.K. participated to the luminescence measurements, F.L. and F.C. contributed on the synthesis and characterization of the particles, S.P. conceptualized, analyzed the data, wrote the article. All authors had given approval to the final version of the manuscript. This work was supported by Seaborough Research BV, under the umbrella of a Eurostars grant (Project E! 12268 EUROLED), Ecole Normale Supérieure de Lyon, CNRS and University Lyon 1. The authors thank The Département de Chimie Moléculaire, Université Grenoble Alpes, for providing resources to perform an EPR measurement at Helium temperature. Pascal Bargiela of IRCELYON was thanked for XPS analysis.

Conflict of Interest

The authors declare no conflict of interest.

Data Availability Statement

The data that support the findings of this study are available in the supplementary material of this article.

Keywords

cerium, glycothermal, photoluminescence, ultra-small nanoparticles, yttrium aluminum garnet

Received: December 22, 2022
Revised: February 27, 2023
Published online:

[1] A. Cantarano, A. Ibanez, G. Dantelle, *Frontiers in Materials* **2020**, *7*.
[2] A. C. Berends, M. A. van de Haar, M. R. Krames, *Chem. Rev.* **2020**, *120*, 13461.
[3] S. Hosokawa, Y. Tanaka, S. Iwamoto, M. Inoue, *Adv. Sci. Technol.* **2006**, *45*, 691.
[4] R. Kasuya, T. Isobe, H. Kuma, *J. Alloys Compd.* **2006**, *408-412*, 820.
[5] H. F. Gaiser, A. Kuzmanoski, C. Feldmann, *RSC Adv.* **2019**, *9*, 10195.
[6] M. R. Krames, O. B. Shchekin, R. Mueller-Mach, G. O. Mueller, L. Zhou, G. Harbers, M. G. Craford, *J. Disp. Technol.* **2007**, *3*, 160.
[7] M. A. van de Haar, A. C. Berends, M. R. Krames, L. Chepyga, F. T. Rabouw, A. Meijerink, *J. Phys. Chem. Lett.* **2020**, *11*, 689.
[8] R. Asakura, T. Isobe, *J. Mater. Sci.* **2013**, *48*, 8228.
[9] Y. Y. Zhao, X. Y. Zhang, D. L. Yan, G. S. Zhu, C. H. Liang, X. Q. Yang, H. R. Xu, A. B. Yu, *J. Am. Ceram. Soc.* **2018**, *101*, 1801.
[10] M. Inoue, H. Otsu, H. Kominami, T. Inui, *J. Alloys Compd.* **1995**, *226*, 146.
[11] M. Odziomek, F. Chaput, F. Lerouge, M. Sitarz, S. Parola, *J. Mater. Chem. C* **2017**, *5*, 12561.
[12] M. Nyman, L. E. Shea-Rohwer, J. E. Martin, P. Provencio, *Chem. Mater.* **2009**, 1536.
[13] Y. Kamiyama, T. Hiroshima, T. Isobe, T. Koizuka, S. Takashima, *J. Electrochem. Soc.* **2010**, *157*, J149.
[14] S. J. Lim, M. U. Zahid, P. Le, L. Ma, D. Entenberg, A. S. Harney, J. Condeelis, A. M. Smith, *Nat. Commun.* **2015**, *6*, 8210.
[15] B. R. Sutherland, E. H. Sargent, *Nat. Photonics* **2016**, *10*, 295.
[16] D. Haranath, H. Chander, P. Sharma, S. Singh, *Appl. Phys. Lett.* **2006**, *89*, 173118.
[17] A. Revaux, G. Dantelle, N. George, R. Seshadri, T. Gacoin, J. P. Boilot, *Nanoscale* **2011**, *3*, 2015.
[18] A. Wiatrowska, W. Keur, C. Ronda, *J Lumin* **2017**, *189*, 9.
[19] G. Dantelle, D. Testemale, E. Homeyer, A. Cantarano, S. Kodjikian, C. Dujardin, J.-L. Hazemann, A. Ibanez, *RSC Adv.* **2018**, *8*, 26857.
[20] P. Schlotter, R. Schmidt, J. Schneider, *Appl. Phys. A* **1997**, *64*, 417.
[21] Q. Li, L. Gao, D. Yan, *Mater. Chem. Phys.* **2000**, *64*, 41.
[22] M. Borlaf, M. Frankowska, W. W. Kubiak, T. Graule, *Mater. Res. Bull.* **2018**, *100*, 413.
[23] W. Jastrzębski, M. Sitarz, M. Rokita, K. Bułat, *Spectrochim. Acta, Part A* **2011**, *79*, 722.
[24] S. Lucas, E. Champion, D. Bregiroux, D. Bernache-Assollant, F. Audubert, *J. Solid State Chem.* **2004**, *177*, 1302.
[25] Y. Nakazaki, M. Inoue, *J. Phys. Chem. Solids* **2004**, *65*, 429.
[26] A. C. Palke, J. F. Stebbins, L. A. Boatner, *Inorg. Chem.* **2013**, *52*, 12605.
[27] B. Shao, Y. Feng, S. Zhao, S. Yuan, J. Huo, W. Lu, H. You, *Inorg. Chem.* **2017**, *56*, 6114.
[28] R. Yang, J. Qin, M. Li, Y. Liu, F. Li, *CrystEngComm* **2011**, *13*, 7284.
[29] S. Peter, M. Richards, Q. Fang, A. Kitai, *Mater. Chem. Phys.* **2022**, *277*, 125497.
[30] C. Canevail, M. Mattoni, F. Morazzoni, R. Scotti, M. Casu, A. Musinu, R. Krsmanovic, S. Polizzi, A. Speghini, M. Bettinelli, *J. Am. Chem. Soc.* **2005**, *127*, 14681.
[31] M. S. Pathak, N. Singh, V. Singh, S. Watanabe, T. K. G. Rao, J.-K. Lee, *Mater. Res. Bull.* **2018**, *97*, 512.
[32] W. O. Milligan, D. F. Mullica, *Inorganica Chemica Acta* **1982**, *60*, 39.
[33] G. W. Beall, L. A. Boatner, *J. Inorg. Nucl. Chem.* **1981**, *43*, 101.
[34] A. Nakatsuka, A. Yoshiasa, T. Yamanaka, *Acta Crystallogr. B* **1999**, *55*, 266.
[35] M. Inoue, T. Nishikawa, H. Otsu, H. Kominami, T. Inui, *J. Am. Ceram. Soc.* **1998**, *81*, 1173.
[36] R. Shannon, *Acta Crystallogr. A* **1976**, *32*, 751.
[37] J. T. S. Irvine, A. R. West, *Solid State Ionics* **1990**, *40-41*, 896.
[38] J. Ueda, S. Tanabe, *Opt. Mater.: X* **2019**, *1*, 100018.
[39] P. E. R. Blanchard, R. G. Cavell, A. Mar, *J. Solid State Chem.* **2010**, *183*, 1477.
[40] D. Kuo, W. M. Kriven, *J. Am. Ceram. Soc.* **1995**, *78*, 3121.
[41] C. Frontera, J. Rodriguez-Carvajal, *Physica B Condens Matter* **2003**, *335*, 219.